Anomalous Net Biome Exchange over Amazonian Rainforests Induced by the 2015/16 El Niño: Temperature-dominated Total Flux but Soil Dryness-shaped Spatial Pattern

Jun Wang[1,2*], Ning Zeng[3], Meirong Wang[4,2], Fei Jiang[1], Frédéric Chevallier[5], Sean Crowell[6], Wei He[1], Matthew S. Johnson[7], Junjie Liu[8], Zhiqiang Liu[9], Scot M. Miller[10], Sajeev Philip[11], Hengmao Wang[1], Mousong Wu[1], Weimin Ju[1], Shuzhuang Feng[1], Mengwei Jia[1]

[1]Frontiers Science Center for Critical Earth Material Cycling/International Institute for Earth System Science, Nanjing University, Nanjing 210023, China

[2]Key Laboratory of Meteorological Disaster (KLME), Ministry of Education & Collaborative Innovation Center on Forecast and Evaluation of Meteorological Disasters (CIC-FEMD), Nanjing University of Information Science & Technology, Nanjing, China

[3]Department of Atmospheric and Oceanic Science and Earth System Interdisciplinary Center, University of Maryland, College Park, MD, USA

[4]Joint Center for Data Assimilation Research and Applications/Joint International Research Laboratory of Climate and Environment Change (ILCEC), Nanjing University of Information Science and Technology, Nanjing, China

[5]Laboratoire des Sciences du Climat et de L'Environnement, LSCE/IPSL, CEA-CNRS-UVSQ, Université Paris-Saclay, 91191 Gif-sur-Yvette, France

[6]University of Oklahoma, Norman, OK, USA

[7]Earth Science Division, NASA Ames Research Center, Moffett Field, CA, USA.

[8]Jet Propulsion Laboratory, California Institute of Technology, Pasadena, CA, USA

[9]State Key Laboratory of Numerical Modelling for Atmospheric Sciences and Geophysical Fluid Dynamics, Institute of Atmospheric Physics, Chinese Academy of Sciences, Beijing, China

[10]Department of Environmental Health and Engineering, Johns Hopkins University, Baltimore, MD 21218, USA

[11]Centre for Atmospheric Sciences, Indian Institute of Technology Delhi, New Delhi, India

Corresponding author: Jun Wang (wangjun@nju.edu.cn)

Key Points:

(1) NBE anomalies over Amazonian rainforests induced by the 2015/16 El Niño were investigated based on thirteen atmospheric inversion models

(2) The total positive NBE anomaly was estimated at about 0.4 PgC yr^{-1} in 2015/16, predominantly caused by higher temperature

(3) The spatial pattern of NBE anomaly was regulated by soil water with larger anomalous NBE over the eastern and northern Amazonian rainforests

Abstract

The magnitude and spatial pattern of anomalous net biome exchange (NBE) induced by the 2015/16 El Niño over Amazonian rainforests remains uncertain. We here investigated them using multi-model posterior NBE products in the Orbiting Carbon Observatory-2 (OCO-2) version 10 modeling intercomparison project (MIP). We find that relative to the annual NBE average in 2017/18, larger anomalous carbon release occurred over the eastern and northern Amazonian rainforests in 2015/16, with a total flux of approximately 0.4 PgC yr^{-1} after assimilating satellite-observed column CO_2 concentrations (XCO_2) over land. This total positive NBE anomaly was dominated by higher temperature with its contributions of approximately 60% in LNLG and 54% in LNLGIS experiments, respectively. However, its anomalous spatial pattern was predominantly determined by soil dryness with the highest spatial partial correlation coefficient. We believe that atmospheric inversions assimilating satellite-observed XCO_2 can better decipher regional carbon flux variations although discrepancies exist among different models.

Plain Language Summary

We investigated the magnitude and spatial pattern of anomalous net biome exchange (NBE) induced by the 2015/16 extreme El Niño over Amazonian rainforests, based on multi-model posterior NBE products in the Orbiting Carbon Observatory-2 (OCO-2) version 10 modeling intercomparison project (MIP). The multi-model ensemble NBE anomalies showed larger carbon release over the eastern and northern Amazonian rainforests, which was predominantly regulated by soil water availability. Further, we estimated a total anomalous carbon flux of approximately 0.4 PgC yr^{-1}. Linear decomposition analysis revealed that this total NBE anomaly was controlled, however, by higher temperature. We believe that these atmospheric inversions assimilating satellite-observed XCO_2 can better decipher regional carbon flux variations associated with their underlying mechanisms.

Keywords: net biome exchange, Amazonian rainforests, OCO-2 MIP, 2015/16 El Niño, climate drivers

1. Introduction

The interannual variability of tropical and global land-atmosphere carbon flux, linked to the El Niño-Southern Oscillation (ENSO), has been the topic of many scientific studies [*Bowman et al.*, 2017; *Jung et al.*, 2017; *Liu et al.*, 2017; *Palmer et al.*, 2019; *Peylin et al.*, 2013; *Piao et al.*, 2020; *Rodenbeck et al.*, 2018; *J Wang et al.*, 2016; *J Wang et al.*, 2018b; *Zeng et al.*, 2005]. In particular, these year-to-year variations reveal how terrestrial ecosystems cope with the abiotic stresses induced by ENSO events, and may shed some light on the future changes of terrestrial carbon cycle under greenhouse warming [*Arora et al.*, 2020; *Cox et al.*, 2018; *Friedlingstein et al.*, 2006]. The tropical rainforests, with the largest areas located over Amazonia, make the second largest contribution (approximately 28%) to the interannual variability of global net biome productivity (NBP) based on the TRENDY multi-model simulations [*Ahlstrom et al.*, 2015]. Amazonia has been long recognized as a hot spot of carbon cycle research due to its interannual anomalies [*Koren et al.*, 2018; *Phillips et al.*, 2009; *van Schaik et al.*, 2018] and long-term changes [*Cox et al.*, 2004; *Gatti et al.*, 2021; *Green et al.*, 2020].

During the recent 2015/16 extreme El Niño, the gross primary productivity (GPP) and solar-induced fluorescence (SIF) were suppressed over Amazonia due to anomalously higher temperature and lower soil moisture [*Koren et al.*, 2018; *van Schaik et al.*, 2018]; however, forest canopy greenness showed a small increase due to enhanced solar radiation [*Yang et al.*, 2018]. As for the net carbon flux to atmosphere, an inverse modeling study suggested approximately 0.5 PgC release anomaly from Amazonia from September 2015 to June 2016, by assimilating in situ

observations and vertical profile data in the Amazon [*Gloor et al.*, 2018]. *Liu et al.* [2017] suggested 0.9±0.29 Pg more carbon into atmosphere in 2015 than in the previous La Niña year 2011 over tropical South America, which was estimated by an atmospheric inversion constrained with CO_2 observations from the Orbiting Carbon Observatory-2 (OCO-2), SIF, and carbon monoxide (CO) observations from Measurements of Pollution in the Troposphere (MOPITT). However, these two studies did not show the spatial characteristics of anomalous net land-atmosphere carbon flux, and related climate drivers were mainly qualitatively discussed.

Recently, net biome exchange (NBE) from the OCO-2 version 10 modeling intercomparison project (MIP) have become available. The NBE is sum of net ecosystem exchange (NEE) and wildfire-induced carbon emissions (F_{fire}). We expect that these models can better capture the characteristics of regional carbon flux anomalies after assimilating satellite-observed XCO_2 data, compared with the traditional atmospheric inversions used in previous studies [*Bastos et al.*, 2018; *J Wang et al.*, 2018a]. Therefore, based on the posterior NBE optimized by these multiple inversion models, we revisit the magnitude and spatial pattern of anomalous NBE over Amazonian rainforests induced by the extreme 2015/16 El Niño. Further, we will attempt to quantitatively reveal the contributions of different climate drivers.

2. Materials and methods

2.1 Posterior NBE from multiple atmospheric inversion models

This study used the posterior NBE optimized by thirteen atmospheric inversion models (Table 1) from the OCO-2 v10 MIP, which is an international collaboration of CO_2 flux inversion modelers. Modelers performed a standard suit of inversion experiments, constrained by CO_2 observations

from OCO-2 and in situ [*Byrne et al.*, 2022; *Crowell et al.*, 2019; *Peiro et al.*, 2022], reported results for years 2015–2020. We here adopted results from three experiments, including: (1) IS: Assimilation of in situ CO_2 measurements from an international observational network; (2) LNLG: Assimilation of OCO-2 ACOS v10 land nadir and land glint XCO_2 retrievals [*OCO-2 Science Team/Gunson and Eldering*, 2020]; (3) LNLGIS: Assimilation of in situ CO_2 measurements and OCO-2 ACOS v10 land nadir and land glint XCO_2 retrievals. For each inversion experiment, modelers prescribed a common fossil fuel emission, but adopted independent other prior surface carbon flux estimates (net ecosystem exchange, ocean, and wildfire emissions) [*Peiro et al.*, 2022]. The common fossil fuel emission adopted the Open-source Data Inventory for Anthropogenic CO_2 (ODIAC) emission data product with the monthly gridded 1°×1° emissions up to 2019 [*Oda et al.*, 2018] and extrapolated emissions in 2020 with additional information from the Carbon Monitor (CM) emission product (https://carbonmonitor.org/). Specifications for each atmospheric inversion model are listed in Table 1.

The posterior NBE provided by the OCO-2 v10 MIP community has a horizontal resolution at 1°×1°. In order to lower the noise in space to some extent, we in this study performed the analyses at 2.5°×2.5° which were interpolated by using the Climate Data Operators (CDO) tool based on the approach of the first order conservative remapping scheme [*Jones*, 1999]:

$$\overline{F_k} = \frac{1}{A_k} \int f\, A \tag{1}$$

where $\overline{F_k}$ represents the area-averaged destination terrestrial carbon flux. A_k is the area of grid k, and f is the original carbon flux. Additionally, we also provide the main results at 1°×1° in the supplementary (Fig. S1). By comparison, results at these two resolutions are consistent.

Table 1. Specifications for atmospheric inversion models participated in OCO-2 v10 MIP.

No.	Inverse model	Inverse method	Transport model	Meteorology	Resolution	References
1	Ames	4D-Var	GEOS-Chem	MERRA-2	4°×5°	*Philip et al.* [2022]
2	Baker	4D-Var	PCTM	MERRA-2	4°×5°	*Baker et al.* [2006]
3	CAMS	Variational	LMDZ	ERA5	1.9 x 3.75	*Chevallier et al.* [2005]
4	CMS-Flux	4D-Var	GEOS-Chem	MERRA-2	4°×5°	*J Liu et al.* [2021]
5	COLA	EnKF	GEOS-Chem	MERRA-2	4°×5°	*Z Liu et al.* [2022]
6	CSU	Bayesian synthesis	GEOS-Chem	MERRA-2	4°×5°	*Schuh et al* .[2010]
7	CT	EnKF	TM5	ERA5	2°×3° / 1° ×1°	*Jacobson et al.* [2020]
8	JHU	geostatistical/4D-Var	GEOS-Chem	MERRA-2	4°×5°	*Chen et al.* [2021]
9	NIES	4D-Var	NIES-TM/ FLEXPART	ERA-5/JRA-55	3.75°× 3.75° / 0.1°×0.1°	*Maksyutov et al.* [2021]
10	OU	4D-Var	TM5	ERA-Interim	4°×6°	*Crowell et al.* [2018]
11	TM5-4DVar	4D-Var	TM5	ERA-Interim	2°× 3°	*Basu et al.* [2013]
12	UT	4D-Var	GEOS-Chem	GEOS-FP	4°×5°	*Deng et al.* [2016]
13	WOMBAT	Synthesis with MCMC	GEOS-Chem	MERRA-2	2°×2.5°	*Zammit-Mangion et al.* [2022]

2.2 Meteorological and land cover datasets

We used land surface air temperature from the Climatic Research Unit gridded Time Series (CRU TS) v.4.05 at 0.5°×0.5° [*Harris et al.*, 2020], which was generated by the interpolation of monthly climate anomalies from global weather station observations.

The soil dryness condition was indicated by the terrestrial water storage (TWS) from a reconstructed product of the Gravity Recovery and Climate Experiment (GRACE-REC) which was generated by a statistical model trained with GRACE observations [*Humphrey and Gudmundsson*, 2019]. The GRACE-REC product was provided in six reconstructed TWS datasets

of 100 ensemble members each at both daily and monthly timesteps over the period of 1901 to present with a 0.5°×0.5° resolution, based on two different GRACE products (JPL and GSFC mascons) and three meteorological forcing datasets. Considering the time span and product evaluation [*Humphrey et al.*, 2021], this study adopted the ensemble mean of the GSFC-ERA5 monthly product which had the time span from January 1979 to July 2019. In order to independently assess this product, we further compared it with other three soil moisture products, and found that they consistently have high spatial correlation coefficients in pairs over Amazonian rainforests (Table S1).

The vapor pressure deficit (VPD) was first calculated based on the ERA5 hourly data on single levels at 0.25°×0.25° [*Hersbach et al.*, 2020]. Specifically, we used the following equations:

$$VPD = (SVP - AVP)/1000 \tag{2}$$

where SVP and AVP represented the saturated and actual vapor pressure in pascals, respectively. The derived VPD was in kPa. And SVP and AVP were calculated with a commonly used parameterization as follows:

$$\begin{cases} SVP = 610.78 \times e^{\frac{17.27T_{as}}{T_{as}+237.29}} \\ AVP = 610.78 \times e^{\frac{17.27T_{d}}{T_{d}+237.29}} \end{cases} \tag{3}$$

where T_{as} and T_d were surface air temperature and dew-point temperature in degrees Celsius, respectively. Then we aggregated calculated hourly VPD into monthly and annual averages.

The Oceanic Niño Index (ONI) was adopted here to infer the ENSO conditions, which was the running 3-month area-averaged sea surface temperature anomalies (SSTA) for the Niño3.4 region (5°S–5°N, 120°W–170°W).

In order to retrieve the domain of Amazonian rainforests in this study, we adopted the Terra and Aqua combined Moderate Resolution Imaging Spectroradiometer (MODIS) Land Cover Climate

Modeling Grid (CMG) (MCD12C1) Version 6 data product [*Friedl et al*., 2015], which were also consistently resampled into 2.5°×2.5° by the approach of the largest area fraction remapping.

2.3 Calculation of NBE and climate anomalies

According to the ONI table (https://origin.cpc.ncep.noaa.gov/products/analysis_monitoring/ensostuff/ONI_v5.php), an extreme El Niño occurred in 2015/16 with the maximum ONI of 2.6℃, followed by two weak La Niña events in 2016/17 and 2017/18. Owing to the short period of posterior NBE products, the climatology cannot be accurately derived which can be greatly influenced by the extreme El Niño event. Hence, we derived the anomalies of NBE and climate factors in each grid over Amazonian rainforests by calculating the difference between the averages during 2015/16 and those during 2017/18. This simple method is analogous to the approach used by *Liu et al*. [2017] in which they calculated the anomaly in 2015 relative to the value in 2011.

2.4 Contributions of climate drivers to NBE anomalies

Surface air temperature, soil moisture, and VPD are the main climate factors, driving the interannual variability of land-atmosphere carbon flux [*He et al.*, 2022; *Humphrey et al.*, 2018; *Jung et al.*, 2017; *J Wang et al.*, 2016; *W Wang et al.*, 2013]. In order to quantitatively calculate the contributions of these three climate drivers to NBE anomalies over Amazonian rainforests induced by the 2015/16 extreme El Niño, we calculated their second-order partial correlation coefficients and adopted the multiple linear regression to decompose NBE anomalies in space. To derive the second-order partial correlation coefficient, we first calculated the first-order partial

correlation (denoted as $r_{12,3}$) which is a measure of the relationship between variable X_1 and X_2, controlling for the other variable X_3:

$$r_{12,3} = \frac{r_{12} - r_{13}r_{23}}{\sqrt{(1-r_{13}^2)(1-r_{23}^2)}} \quad (4)$$

Then, we can derive the second-order partial correlation (denoted as $r_{12,34}$) which is a measure of the relationship between variable X_1 and X_2, controlling for the other two variables X_3 and X_4:

$$r_{12,34} = \frac{r_{12,3} - r_{14,3}r_{24,3}}{\sqrt{(1-r_{14,3}^2)(1-r_{24,3}^2)}} \quad (5)$$

Decomposition of NBE anomalies in space into individual contributions was achieved as follows:

$$NBE = \beta^T T + \beta^{SM} SM + \beta^{VPD} VPD + \varepsilon \quad (6)$$

where β^T, β^{SM}, and β^{VPD} represent the sensitivities of NBE to temperature, soil moisture, and VPD anomalies, respectively. This method needs to assume the same climate sensitivities in space. Of course, it seems reasonable because we here focus on Amazonian rainforests (broadleaf forests in MODIS land cover). The term of ε represents the residual. We can further rewrite Equation 6 using the more compact symbols:

$$NBE = NBE^T + NBE^{SM} + NBE^{VPD} + \varepsilon \quad (7)$$

where NBE^T, NBE^{SM}, and NBE^{VPD} denote the NBE anomalies induced by temperature, soil moisture, and VPD, respectively.

3. Results and discussion

3.1 Anomalous posterior NBE over Amazonian rainforests

The geographical distributions of calculated annual NBE anomalies over Amazonian rainforests related to the extreme 2015/16 El Niño are presented in Fig. 1. The ensemble NBE anomalies in OCO-2 v10 MIP Prior were nearly neutral (Fig. 1a), indicating that the obvious posterior NBE anomalies originated from the information of the in situ and satellite-observed atmospheric CO_2 concentration. The ensemble NBE anomalies constrained by in situ CO_2 observations (IS experiment) showed moderate anomalous carbon release (positive values) with the slightly stronger magnitudes over the eastern Amazonia (Fig. 1b). Compared to the limited stations of in situ CO_2 observations, the OCO-2 XCO_2 product largely increases the coverage of atmospheric CO_2 observations over the tropical South America, even though it is limited to clear areas and much hampered by the cosmic rays from the South Atlantic Anomaly [*Byrne et al.*, 2022]. The ensemble posterior NBE anomalies in LNLG and LNLGIS had the similar spatial patterns, showing the much stronger carbon release over the eastern and northern parts of Amazonian rainforests (Figs. 1c and d).

More specifically, longitudinal changes of NBE anomalies showed that although large inter-model spread existed, the ensemble posterior NBE anomalies in LNLG and LNLGIS had significantly stronger carbon release (approximately double, 0.05 PgC yr^{-1}) from 57.5°W to 67.5°W than results in IS ($p < 0.1$) (Fig. 1e). The ensemble NBE anomalies over the entire Amazonian rainforests were 0.02±0.09 PgC yr^{-1} in Prior and 0.28±0.22 PgC yr^{-1} in IS. After assimilating OCO-2 XCO_2 observations over land, the total ensemble NBE anomalies were 0.42±0.14 PgC yr^{-1} in LNLG and 0.39±0.15 PgC yr^{-1} in LNLGIS, showing their enhanced carbon release by approximately 50% and 39%, respectively, relative to the estimated magnitude in IS

(Fig. 1f). The NBE anomaly composed of NEE and F_{fire} anomalies, in which F_{fire} anomaly was estimated at 0.05 PgC yr^{-1} based on GFEDv4.1s product (Fig. 1f), suggesting the dominant contribution of NEE to NBE anomaly. Additionally, the inter-model spread in the total NBE anomalies in IS was obviously larger than that in LNLG, indicating that larger discrepancies existed in assimilating in situ observations in these atmospheric inversion models.

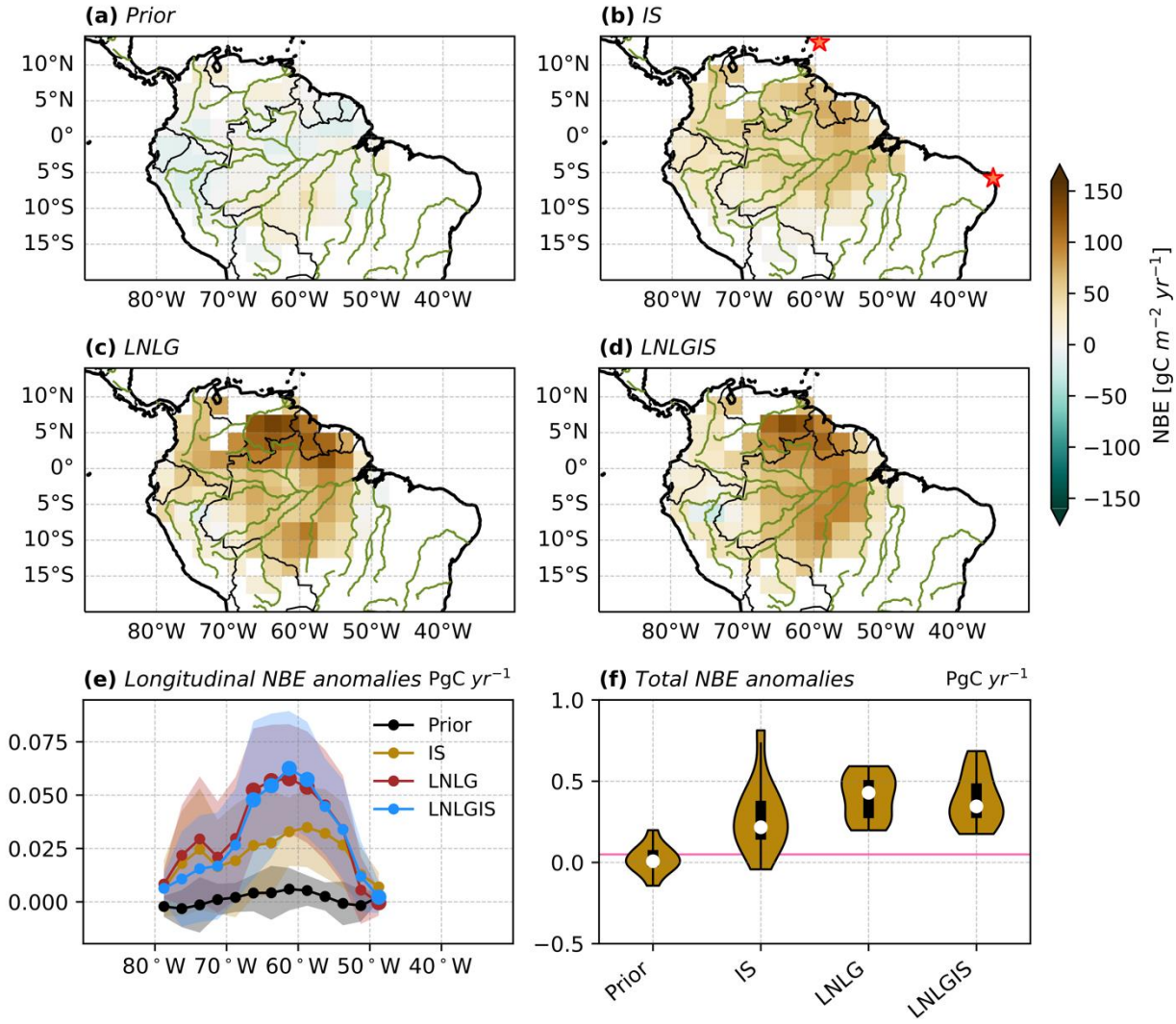

Figure 1. Geographical distributions of anomalous annual net biome exchange (NBE) induced by the 2015/16 El Niño over the Amazonian rainforests. Prior (**a**) and posterior ensemble NBE anomalies at 2.5°×2.5° grids in inversion experiments of IS (**b**), LNLG (**c**), and LNLGIS (**d**) in the

OCO-2 v10 MIP. These annual anomalies were calculated by their differences between averaged annual NBE during 2015–2016 and that during 2017–2018. The unit of NBE anomalies in (**a–d**) is gC m^{-2} yr^{-1}. The red stars in (**b**) show the locations of in situ observations in this focused domain. (**e**) Longitudinal total ensemble NBE anomalies in the unit of PgC yr^{-1}. The shaded areas represent the standard deviation (1-σ) of multi-model inversion results in each experiment. The bigger dots in LNLG and LNLGIS represent that they are significantly different from those in IS with statistical significance at $p < 0.1$ level estimated by the two-sided Student's *t* test. (**f**) Violin plots of multi-model total NBE anomalies over entire Amazonia rainforests. The total NBE is in the unit of PgC yr^{-1}. The red line represents the anomalous carbon emissions induced by wildfires estimated by the GFEDv4.1s dataset.

3.2 Climate drivers

Interannual NBE anomalies were predominantly controlled by climate variations, mainly by temperature, soil moisture, and VPD [*He et al.*, 2022; *Humphrey et al.*, 2018; *Jung et al.*, 2017; *J Wang et al.*, 2016; *W Wang et al.*, 2013; *Zeng et al.*, 2005]. Regression analysis revealed that 1K increase of ONI in the preceding December can increase the annual temperature by 0.1 K (R^2 = 0.51, $p < 0.01$), enhance VPD by 0.02 kPa ($R^2 = 0.41$, $p < 0.01$), and reduce TWS by 0.16 TtH_2O ($R^2 = 0.84$, $p < 0.01$) over the entire Amazonian rainforests (Fig. 2a). Accordingly, the climate conditions showed the higher temperature and VPD, and drier soil moisture in 2015/16, but in contrast the lower temperature and VPD, and wetter soil moisture in 2017/18 (Fig. 2a). Relative to the averages in 2017/18, temperature showed the positive anomalies over the entire Amazonian rainforests with the higher temperature anomalies located over the central part (Fig. 2b), which can potentially inhibit the vegetation photosynthesis and enhance soil respiration [*Crowther et al.*,

256 2016; *Zeng et al.*, 2005]. The soil and atmospheric dryness mainly occurred over the northeastern
257 Amazonia albeit with differences in their spatial patterns (Figs. 2c and d), which both can reduce
258 vegetation photosynthesis [*Lopez et al.*, 2021; *Stocker et al.*, 2019; *Werner et al.*, 2021; *Yuan et*
259 *al.*, 2019]. Therefore, these three climate drivers simultaneously contributed to the positive NBE
260 anomalies (Figs. 1c and d).
261

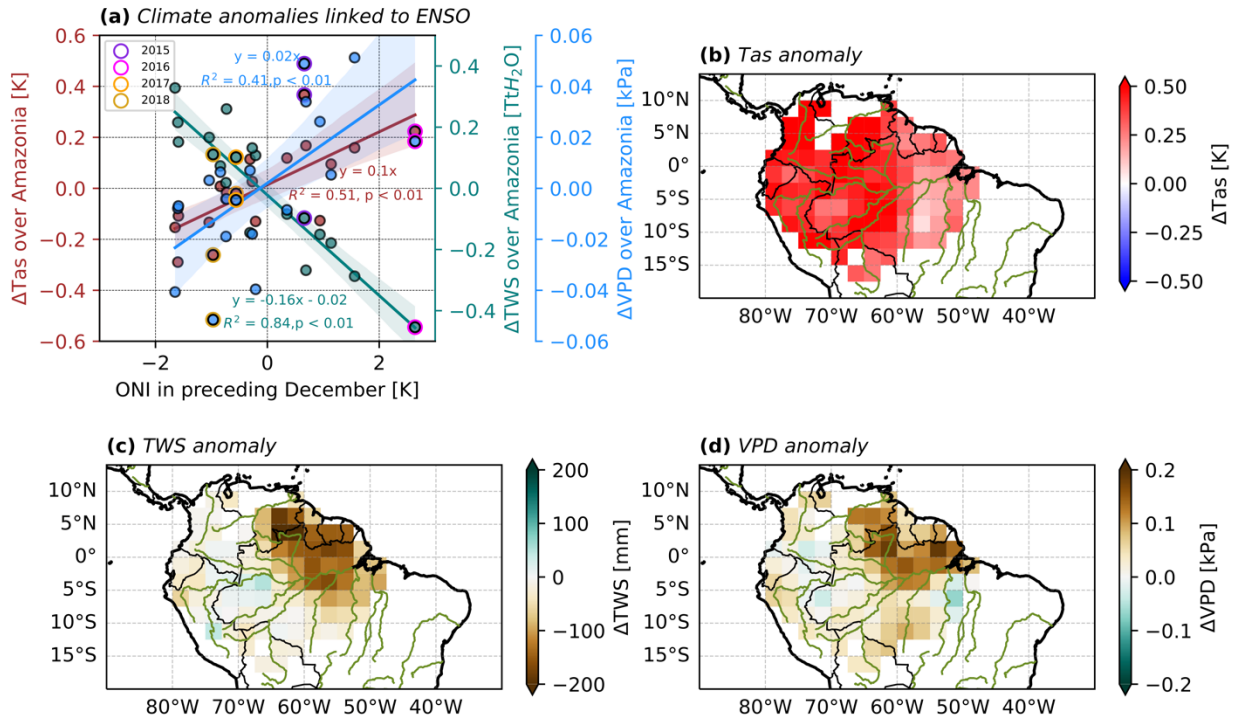

262

263 **Figure 2.** Anomalous climate factors over the Amazonian rainforests. (**a**) Relationship between
264 detrended climate anomalies, including surface air temperature (Tas, red), terrestrial water storage
265 (TWS, green), and vapor pressure deficit (VPD, blue), and Oceanic Niño Index (ONI) in the
266 preceding December from 2000 to 2018. Anomalous climate patterns of Tas (**b**), TWS (**c**), and
267 VPD (**d**) linked to the 2015/16 El Niño were consistently calculated by their differences between
268 annual mean during 2015–2016 and that during 2017–2018.
269

In space, the stronger positive ensemble NBE anomalies over the eastern and northern parts of Amazonian rainforests (Figs. 1c and d) were visually more consistent with the pattern of TWS anomaly (Fig. 2c). Quantitatively, the partial correlation coefficients between gridded NBE and TWS anomalies, controlling for the temperature and VPD, reached −0.37 (confidence interval from −0.53 to −0.18, $p < 0.05$) in LNLG and −0.44 (confidence interval from −0.59 to −0.25, $p < 0.05$) in LNLGIS, respectively, which were followed by the partial correlation coefficients between NBE and temperature anomalies with 0.35 (confidence interval from 0.15 to 0.52, $p < 0.05$) in LNLG and 0.19 (confidence interval from −0.02 to 0.38, $p = 0.08$) in LNLGIS, respectively (Fig. 3a). Consistently, these higher values of the partial correlation coefficients between NBE and TWS anomalies both in LNLG and LNLGIS confirmed that TWS anomalies predominantly shaped the anomalous NBE pattern related to the extreme 2015/16 El Niño.

However, linear decomposition analysis (Equation 7) revealed that the total NBE anomaly over the entire Amazonian rainforests of 0.42±0.14 PgC yr^{-1} in LNLG composed of 0.25±0.18 PgC yr^{-1} induced by temperature, 0.11±0.11 PgC yr^{-1} induced by TWS, and 0.05±0.12 PgC yr^{-1} induced by VPD, respectively, with the approximately 60% contribution from temperature (Fig. 3b). Similarly, the total NBE anomaly of 0.39±0.15 PgC yr^{-1} in LNLGIS was predominantly contributed to by temperature-induced anomaly of 0.21±0.16 PgC yr^{-1} with the approximately 54% contribution. Our result of temperature-dominated total NBE anomaly was different from the finding by *Liu et al.* [2017] that the NBE anomaly over tropical South America was largely controlled by extreme precipitation anomalies, where of course there were some differences in the anomaly calculation and research domain.

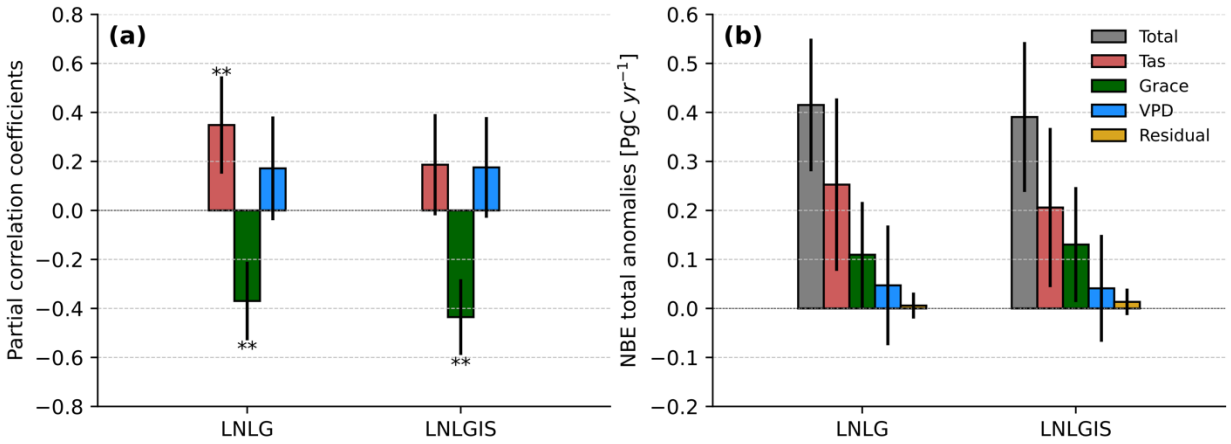

Figure 3. Associations between ensemble annual NBE anomalies and climate factors over Amazonian rainforests. (**a**) Partial correlation coefficients in space between ensemble annual NBE anomalies and individual climate factor, controlling for the other two factors. The error bars represent 95% parametric confidence intervals. The symbol of ** denotes the statistical significance at $p < 0.05$ level. (**b**) Decomposed contributions of individual climate factors to total NBE anomalies induced by the 2015/16 El Niño over entire Amazonian rainforests. The error bars represent the 1-σ of multi-model inversion results.

3.3 Uncertainty in multi-model inverted NBE anomalies

This study mainly focuses on the multi-model ensemble NBE anomalies, but we should realize that inter-model spread existed in magnitudes and spatial patterns of NBE anomalies (Figs. 3b, S2, and S3). Although these inversion models performed experiments following the same protocols in the OCO-2 v10 MIP, the uncertainties among different models can be mainly attributed to the settings of errors in prior surface carbon fluxes, the errors in the atmospheric transport induced by different transport models and meteorological products used, and choices in the optimization techniques (Table 1) [*Basu et al.*, 2018; *Chevallier et al.*, 2010; *Schuh et al.*, 2019]. Here, a Taylor

diagram for NBE anomalies in individual inversion models from LNLG and LNLGIS relative to their respective ensemble NBE anomalies is presented in Fig. 4. In LNLG, except CT and NIES, most of models show high spatial correlation coefficients with their ensemble NBE anomalies (> 0.30) in which Ames has the highest correlation coefficient of 0.80 ($p < 0.05$). In other words, these models can capture the main characteristics of the spatial pattern of the ensemble NBE anomalies. But most of them have stronger standard deviation in space than that of ensemble NBE anomalies, indicating larger spatial difference of NBE anomalies in these individual models over Amazonian rainforests (Fig. 1 and S2). For example, obvious positive NBE anomalies occurred over northern Amazonia and negative anomalies occurred over southwestern Amazonia in UT (Fig. S2), making it have the highest normalized standard deviation of 4.86. Similar performance is exhibited in LNLGIS. Interestingly, the spatial correlation coefficient in JHU decreased from 0.36 in LNLG to −0.13 in LNLGIS, while correlation coefficient in CT increased from −0.04 in LNLG to 0.42 in LNLGIS. More detailed spatial characteristics of posterior NBE anomalies induced by the extreme 2015/16 El Niño for each model in LNLG and LNLGIS can be referred to in Figs. S1 and S2.

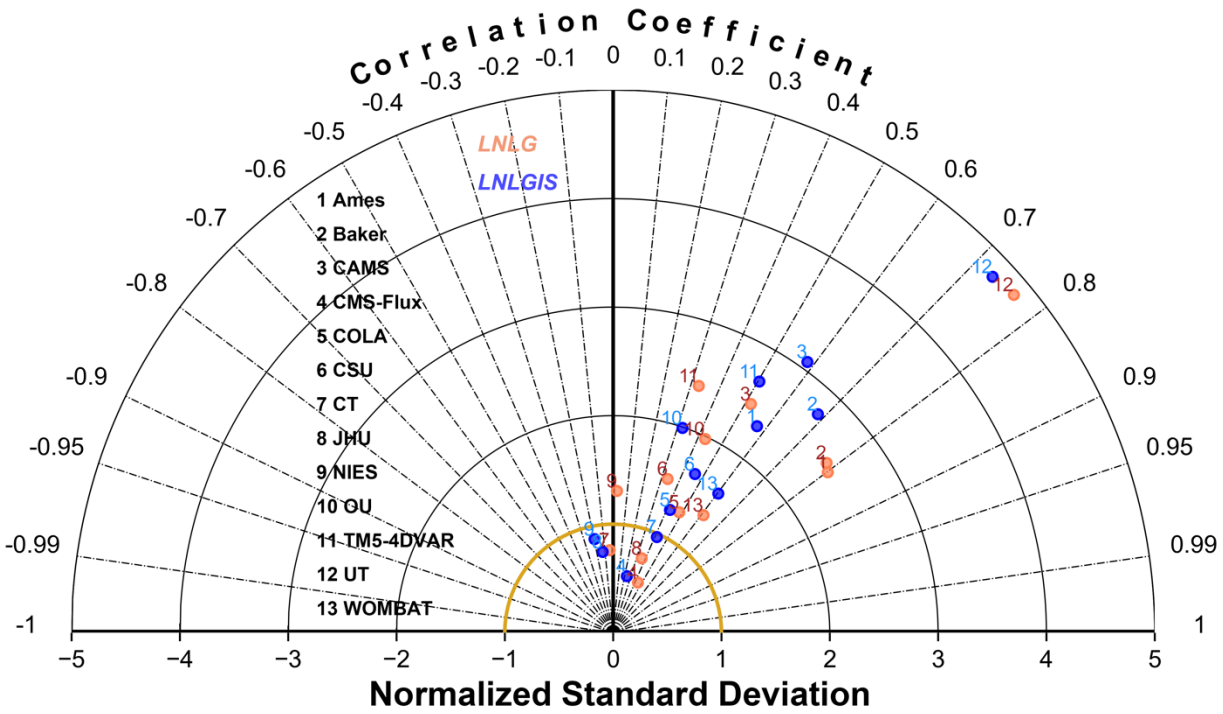

Figure 4. Taylor diagram for NBE anomalies in individual inversion models from LNLG and LNLGIS relative to their respective ensemble NBE anomalies. The values in the arc and x-axis represent the spatial correlation coefficients and normalized standard deviation, respectively. The red and blue dots show the individual inversion result in LNLG and LNLGIS, respectively.

4. Conclusions

Based on the posterior NBE anomalies provided by thirteen atmospheric inversion models participated in OCO-2 v10 MIP, we find a total NBE anomaly of 0.42±0.14 PgC yr^{-1} in LNLG and 0.39±0.15 PgC yr^{-1} in LNLGIS induced by the extreme 2015/16 El Niño relative to the baseline of 2017/18, showing the stronger carbon release over the eastern and northern parts of Amazonian rainforests. These anomalous spatial patterns of NBE in LNLG and LNLGIS were consistently controlled by the soil water availability with the highest partial correlation coefficients

between NBE and TWS of −0.37 ($p < 0.05$) in LNLG and −0.44 ($p < 0.05$) in LNLGIS, respectively. However, linear decomposition analysis suggested the dominant role of temperature in the total NBE anomaly over the entire Amazonian rainforests with its contributions of approximately 60% in LNLG and 54% in LNLGIS, respectively.

Acknowledgements

We gratefully acknowledge the OCO-2 v10 MIP community for access to gridded posterior land-atmosphere carbon flux data. The calculations in this paper have been done on the computing facilities in the High Performance Computing Center (HPCC) of Nanjing University. This study was supported by the National Key Research and Development Program of China (grant nos. 2021YFB3901001 and 2020YFA0607504), the Natural Science Foundation of Jiangsu Province, China (BK20221449), the Research Funds for the Frontiers Science Center for Critical Earth Material Cycling, Nanjing University (0904-14380031), and the open project of Key Laboratory of Meteorological Disaster (KLME), Ministry of Education & Collaborative Innovation Center on Forecast and Evaluation of Meteorological Disasters (CIC-FEMD), Nanjing University of Information Science & Technology (grant no. KLME202203).

Conflict of Interest

The authors declare no competing interests.

Data Availability

The multi-model gridded posterior land-atmosphere carbon flux datasets in OCO-2 v10 MIP are available at https://gml.noaa.gov/ccgg/OCO2_v10mip/index.php. Land surface air temperature

from CRU TS v. 4.05 is available at https://crudata.uea.ac.uk/cru/data/hrg/. GRACE-REC datasets can be accessed at https://figshare.com/articles/dataset/GRACE-REC_A_reconstruction_of_climate_driven_water_storage_changes_over_the_last_century/7670849. The ERA5 hourly data on single levels are stored at https://cds.climate.copernicus.eu/cdsapp#!/dataset/reanalysis-era5-single-levels?tab=form. MODIS land cover dataset of MCD12C1v006 is available at https://lpdaac.usgs.gov/products/mcd12c1v006/. The ONI data are provided at https://origin.cpc.ncep.noaa.gov/products/analysis_monitoring/ensostuff/ONI_v5.php.

References

Ahlstrom, A., et al. (2015), The dominant role of semi-arid ecosystems in the trend and variability of the land CO_2 sink, *Science*, *348*(6237), 895-899.

Arora, V. K., et al. (2020), Carbon–concentration and carbon–climate feedbacks in CMIP6 models and their comparison to CMIP5 models, *Biogeosciences*, *17*(16), 4173-4222.

Baker, D. F., S. C. Doney, and D. S. Schimel (2006), Variational data assimilation for atmospheric CO2, *Tellus B: Chemical and Physical Meteorology*, *58*(5), 359-365.

Bastos, A., et al. (2018), Impact of the 2015/2016 El Nino on the terrestrial carbon cycle constrained by bottom-up and top-down approaches, *Philosophical transactions of the Royal Society of London. Series B, Biological sciences*, *373*(1760).

Basu, S., D. F. Baker, F. Chevallier, P. K. Patra, J. Liu, and J. B. Miller (2018), The impact of transport model differences on CO_2 surface flux estimates from OCO-2 retrievals of column average CO_2, *Atmospheric Chemistry and Physics*, *18*(10), 7189-7215.

Basu, S., et al. (2013), Global CO_2 fluxes estimated from GOSAT retrievals of total column CO_2 *Atmospheric Chemistry and Physics*, *13*(17), 8695-8717.

Bowman, K. W., et al. (2017), Global and Brazilian Carbon Response to El Niño Modoki 2011-2010, *Earth and Space Science*, *4*(10), 637-660.

Byrne, B., et al. (2022), National CO_2 budgets (2015–2020) inferred from atmospheric CO_2 observations in support of the Global Stocktake, *Earth Syst. Sci. Data Discuss.*, *2022*, 1-59.

Chen, Z., et al. (2021), Linking global terrestrial CO_2 fluxes and environmental drivers: inferences from the Orbiting Carbon Observatory 2 satellite and terrestrial biospheric models, *Atmospheric Chemistry and Physics*, *21*(9), 6663-6680.

Chevallier, F., L. Feng, H. Bösch, P. I. Palmer, and P. J. Rayner (2010), On the impact of transport model errors for the estimation of CO_2 surface fluxes from GOSAT observations, *Geophys Res Lett*, *37*(21), n/a-n/a.

Chevallier, F., M. Fisher, P. Peylin, S. Serrar, P. Bousquet, F. M. Bréon, A. Chédin, and P. Ciais (2005), Inferring CO_2 sources and sinks from satellite observations: Method and application to TOVS data, *Journal of Geophysical Research*, *110*(D24).

Cox, P. M., C. Huntingford, and M. S. Williamson (2018), Emergent constraint on equilibrium climate sensitivity from global temperature variability, *Nature*, *553*(7688), 319-322.

Cox, P. M., R. A. Betts, M. Collins, P. P. Harris, C. Huntingford, and C. D. Jones (2004), Amazonian forest dieback under climate-carbon cycle projections for the 21st century, *Theoretical and Applied Climatology*, *78*(1-3), 137-156.

Crowell, S., et al. (2019), The 2015–2016 carbon cycle as seen from OCO-2 and the global in situ network, *Atmospheric Chemistry and Physics*, *19*(15), 9797-9831.

Crowell, S. M. R., S. Randolph Kawa, E. V. Browell, D. M. Hammerling, B. Moore, K. Schaefer, and S. C. Doney (2018), On the Ability of Space-Based Passive and Active Remote Sensing Observations of CO_2 to Detect Flux Perturbations to the Carbon Cycle, *Journal of Geophysical Research: Atmospheres*, *123*(2), 1460-1477.

Crowther, T. W., et al. (2016), Quantifying global soil carbon losses in response to warming, *Nature*, *540*(7631), 104-108.

Deng, F., D. B. A. Jones, C. W. O'Dell, R. Nassar, and N. C. Parazoo (2016), Combining GOSAT XCO_2 observations over land and ocean to improve regional CO_2 flux estimates, *Journal of Geophysical Research: Atmospheres*, *121*(4), 1896-1913.

Friedl, M., D. Sulla-Menashe (2015), *MCD12C1 MODIS/Terra+Aqua Land Cover Type Yearly L3 Global 0.05Deg CMG V006* [Data set]. NASA EOSDIS Land Processes DAAC. Accessed 2022-06-27 from https://doi.org/10.5067/MODIS/MCD12C1.006

Friedlingstein, P., et al. (2006), Climate-carbon cycle feedback analysis: Results from the C^4MIP model intercomparison, *Journal of Climate*, *19*(14), 3337-3353.

Gatti, L. V., et al. (2021), Amazonia as a carbon source linked to deforestation and climate change, *Nature*, *595*(7867), 388-393.

Gloor, E., et al. (2018), Tropical land carbon cycle responses to 2015/16 El Nino as recorded by atmospheric greenhouse gas and remote sensing data, *Philosophical transactions of the Royal Society of London. Series B, Biological sciences*, *373*(1760).

Green, J. K., J. Berry, P. Ciais, Y. Zhang, and P. Gentine (2020), Amazon rainforest photosynthesis increases in response to atmospheric dryness, *Sci Adv*, *6*(47).

Harris, I., T. J. Osborn, P. Jones, and D. Lister (2020), Version 4 of the CRU TS monthly high-resolution gridded multivariate climate dataset, *Sci Data*, *7*(1), 109.

He, B., et al. (2022), Worldwide impacts of atmospheric vapor pressure deficit on the interannual variability of terrestrial carbon sinks, *Natl Sci Rev*, *9*(4), nwab150.

Hersbach, H., et al. (2020), The ERA5 global reanalysis, *Quarterly Journal of the Royal Meteorological Society*, *146*(730), 1999-2049.

Humphrey, V., and L. Gudmundsson (2019), GRACE-REC: a reconstruction of climate-driven water storage changes over the last century, *Earth System Science Data*, *11*(3), 1153-1170.

Humphrey, V., J. Zscheischler, P. Ciais, L. Gudmundsson, S. Sitch, and S. I. Seneviratne (2018), Sensitivity of atmospheric CO_2 growth rate to observed changes in terrestrial water storage, *Nature*, *560*(7720), 628-631.

Humphrey, V., A. Berg, P. Ciais, P. Gentine, M. Jung, M. Reichstein, S. I. Seneviratne, and C. Frankenberg (2021), Soil moisture–atmosphere feedback dominates land carbon uptake variability, *Nature*, *592*(7852), 65-69.

Jacobson, A. R., et al. (2020), CarbonTracker CT2019B, Model published 2020 by NOAA Earth System Research Laboratory, Global Monitoring Division, DOI: 10.25925/20201008.

Jones, P. W. (1999), First- and second-order conservative remapping schemes for grids in spherical coordinates, *Mon Weather Rev*, *127*(9), 2204-2210.

Jung, M., et al. (2017), Compensatory water effects link yearly global land CO_2 sink changes to temperature, *Nature*, *541*(7638), 516-520.

Koren, G., et al. (2018), Widespread reduction in sun-induced fluorescence from the Amazon during the 2015/2016 El Nino, *Philosophical transactions of the Royal Society of London. Series B, Biological sciences*, *373*(1760).

Liu, J., et al. (2017), Contrasting carbon cycle responses of the tropical continents to the 2015-2016 El Nino, *Science*, *358*(6360).

Liu, J., et al. (2021), Carbon Monitoring System Flux Net Biosphere Exchange 2020 (CMS-Flux NBE 2020), *Earth System Science Data*, *13*(2), 299-330.

Liu, Z., N. Zeng, Y. Liu, E. Kalnay, G. Asrar, B. Wu, Q. Cai, D. Liu, and P. Han (2022), Improving the joint estimation of CO_2 and surface carbon fluxes using a Constrained Ensemble Kalman Filter in COLA (v1.0), *Geosci. Model Dev*, 15, 5511-5528.

Lopez, J., D. A. Way, and W. Sadok (2021), Systemic effects of rising atmospheric vapor pressure deficit on plant physiology and productivity, *Glob Chang Biol*.

Maksyutov, S., et al. (2021), Technical note: A high-resolution inverse modelling technique for estimating surface CO_2 fluxes based on the NIES-TM–FLEXPART coupled transport model and its adjoint, *Atmospheric Chemistry and Physics*, *21*(2), 1245-1266.

OCO-2 Science Team/Gunson M., A. Eldering (2020), OCO-2 Level 2 bias-corrected XCO2 and other select fields from the full-physics retrieval aggregated as daily files, Retrospective processing V10r, Greenbelt, MD, USA, Goddard Earth Sciences Data and Information Services Center (GES DISC), 10.5067/E4E140XDMPO2.

Oda, T., S. Maksyutov, and R. J. Andres (2018), The Open-source Data Inventory for Anthropogenic CO_2, version 2016 (ODIAC2016): a global monthly fossil fuel CO_2 gridded emissions data product for tracer transport simulations and surface flux inversions, *Earth System Science Data*, *10*, 87-107.

Palmer, P. I., L. Feng, D. Baker, F. Chevallier, H. Bosch, and P. Somkuti (2019), Net carbon emissions from African biosphere dominate pan-tropical atmospheric CO_2 signal, *Nat Commun*, *10*(1), 3344.

Peiro, H., et al. (2022), Four years of global carbon cycle observed from the Orbiting Carbon Observatory 2 (OCO-2) version 9 and in situ data and comparison to OCO-2 version 7, *Atmospheric Chemistry and Physics*, *22*(2), 1097-1130.

Peylin, P., et al. (2013), Global atmospheric carbon budget: results from an ensemble of atmospheric CO_2 inversions, *Biogeosciences*, *10*(10), 6699-6720.

Philip, S., M. S. Johnson, D. F. Baker, S. Basu, Y. K. Tiwari, N. K. Indira, M. Ramonet, and B. Poulter (2022), OCO-2 Satellite-Imposed Constraints on Terrestrial Biospheric CO_2 Fluxes Over South Asia, *Journal of Geophysical Research: Atmospheres*, *127*(3).

Phillips, O. L., et al. (2009), Drought Sensitivity of the Amazon Rainforest, *Science*, *323*(5919), 1344-1347.

Piao, S. L., X. H. Wang, K. Wang, X. Y. Li, A. Bastos, J. G. Canadell, P. Ciais, P. Friedlingstein, and S. Sitch (2020), Interannual variation of terrestrial carbon cycle: Issues and perspectives, Global Change Biology, 26(1), 300-318.

484 Rodenbeck, C., S. Zaehle, R. Keeling, and M. Heimann (2018), History of El Nino impacts on the
485 global carbon cycle 1957-2017: a quantification from atmospheric CO_2 data, *Philosophical*
486 *transactions of the Royal Society of London. Series B, Biological sciences*, *373*(1760).
487 Schuh, A. E., A. S. Denning, K. D. Corbin, I. T. Baker, M. Uliasz, N. Parazoo, A. E. Andrews,
488 and D. E. J. Worthy (2010), A regional high-resolution carbon flux inversion of North America
489 for 2004, *Biogeosciences*, *7*(5), 1625-1644.
490 Schuh, A. E., et al. (2019), Quantifying the Impact of Atmospheric Transport Uncertainty on CO_2
491 Surface Flux Estimates, *Global Biogeochem Cycles*, *33*(4), 484-500.
492 Stocker, B. D., J. Zscheischler, T. F. Keenan, I. C. Prentice, S. I. Seneviratne, and J. Peñuelas
493 (2019), Drought impacts on terrestrial primary production underestimated by satellite monitoring,
494 *Nat Geosci*, *12*(4), 264-270.
495 van Schaik, E., L. Killaars, N. E. Smith, G. Koren, L. P. H. van Beek, W. Peters, and I. T. van der
496 Laan-Luijkx (2018), Changes in surface hydrology, soil moisture and gross primary production in
497 the Amazon during the 2015/2016 El Nino, *Philosophical transactions of the Royal Society of*
498 *London. Series B, Biological sciences*, *373*(1760).
499 Wang, J., N. Zeng, and M. Wang (2016), Interannual variability of the atmospheric CO_2 growth
500 rate: roles of precipitation and temperature, *Biogeosciences*, *13*(8), 2339-2352.
501 Wang, J., N. Zeng, M. Wang, F. Jiang, H. Wang, and Z. Jiang (2018a), Contrasting terrestrial
502 carbon cycle responses to the 1997/98 and 2015/16 extreme El Niño events, *Earth System*
503 *Dynamics*, *9*(1), 1-14.
504 Wang, J., et al. (2018b), Contrasting interannual atmospheric CO_2 variabilities and their terrestrial
505 mechanisms for two types of El Ninos, *Atmos. Chem. Phys.*, *18*, 10333-10345.
506 Wang, W., P. Ciais, R. Nemani, J. G. Canadell, S. Piao, S. Sitch, M. A. White, H. Hashimoto, C.
507 Milesi, and R. B. Myneni (2013), Variations in atmospheric CO_2 growth rates coupled with
508 tropical temperature, *PNAS*, *110*, 13061-13066.
509 Werner, C., L. K. Meredith, and S. N. Ladd (2021), Ecosystem fluxes during drought and recovery
510 in an experimental forest, *Science*, *374*(6574).
511 Yang, J., H. Tian, S. Pan, G. Chen, B. Zhang, and S. Dangal (2018), Amazon drought and forest
512 response: Largely reduced forest photosynthesis but slightly increased canopy greenness during
513 the extreme drought of 2015/2016, *Glob Chang Biol*, *24*(5), 1919-1934.
514 Yuan, W. P., et al. (2019), Increased atmospheric vapor pressure deficit reduces global vegetation
515 growth, *Sci Adv*, *5*(8).
516 Zammit-Mangion, A., M. Bertolacci, J. Fisher, A. Stavert, M. Rigby, Y. Cao, and N. Cressie
517 (2022), WOMBAT v1.0: a fully Bayesian global flux-inversion framework, *Geosci Model Dev*,
518 *15*(1), 45-73.
519 Zeng, N., A. Mariotti, and P. Wetzel (2005), Terrestrial mechanisms of interannual CO_2 variability,
520 *Global Biogeochemical Cycles*, *19*(1), GB1016.
521